

Upper critical fields and thermally-activated transport of NdFeAsO_{0.7}F_{0.3} single crystal

J. Jaroszynski, F. Hunte, L. Balicas, Youn-jung Jo, I. Raičević, A. Gurevich, and D. C. Larbalestier
National High Magnetic Field Laboratory, Florida State University, Tallahassee, Florida 32310, USA

F. F. Balakirev

National High Magnetic Field Laboratory, Los Alamos National Laboratory, Los Alamos, New Mexico 87545, USA

L. Fang, P. Cheng, Y. Jia, and H. H. Wen

Institute of Physics, Chinese Academy of Sciences, Beijing 100190, People's Republic of China

(Received 14 October 2008; published 21 November 2008)

We present detailed measurements of the longitudinal resistivity $\rho_{xx}(T, H)$ and the upper critical field H_{c2} of NdFeAsO_{0.7}F_{0.3} single crystals in strong dc and pulsed magnetic fields up to 45 and 60 T, respectively. We found that the field scale of H_{c2} is comparable to $H_{c2} \sim 100$ T of high- T_c cuprates. $H_{c2}(T)$ parallel to the c axis exhibits a pronounced upward curvature similar to what was extracted from earlier measurements on polycrystalline LaFeAs(O,F), NdFeAs(O,F), and SmFeAs(O,F) samples. Thus, this behavior of $H_{c2}^\parallel(T)$ is indeed an intrinsic feature of oxypnictides rather than manifestation of vortex lattice melting or granularity. The orientational dependence of $H_{c2}(\theta)$ as a function of the angle θ between H and the c axis shows deviations from the one-band Ginzburg-Landau scaling. The mass anisotropy parameter $\gamma(T) = (m_c/m_{ab})^{1/2} = H_{c2}^\parallel/H_{c2}^\perp$ obtained from these measurements decreases as temperature decreases from $\gamma \approx 9.2$ at 44 K to $\gamma \approx 5$ at 34 K, where \parallel and \perp correspond to H parallel and perpendicular to the ab planes, respectively. Spin-dependent magnetoresistance and nonlinearities in the Hall coefficient suggest contribution to the conductivity from electron-electron interactions modified by disorder reminiscent of that in diluted magnetic semiconductors. The Ohmic resistivity $\rho_{xx}(T, H)$ measured below T_c but above the irreversibility field exhibits a clear Arrhenius thermally-activated behavior $\rho = \rho_0 \exp[-E_a(T, H)/T]$ over 4–5 decades of ρ_{xx} . The activation energy $E_a(T, H)$ has very different field dependencies for $H \parallel ab$ and $H \perp ab$ varying from 4×10^3 K at $H = 0.2$ T to ~ 200 K at $H = 35$ T. We discuss to what extent different pairing scenarios suggested in the literature can manifest themselves in the observed behavior of H_{c2} , using the two-band model of superconductivity in oxypnictides. The results indicate the importance of paramagnetic effects on $H_{c2}(T)$ in oxypnictides, which may significantly reduce $H_{c2}(0)$ as compared to $H_{c2}(0) \sim 200$ – 300 T based on extrapolations of $H_{c2}(T)$ near T_c down to low temperatures.

DOI: [10.1103/PhysRevB.78.174523](https://doi.org/10.1103/PhysRevB.78.174523)

PACS number(s): 74.70.-b, 74.25.Fy, 74.72.-h, 74.81.Bd

I. INTRODUCTION

The recently discovered layered superconducting oxypnictides with high transition temperatures T_c (Ref. 1) are based on alternating structures of FeAs layers and rare-earth oxide (REO) layers. Similar to the high-temperature superconducting cuprates, superconductivity in oxypnictides emerges upon doping of a parent antiferromagnetic state. As the REO planes are doped, the ionically bonded REO donates carriers to the covalently bonded FeAs plane,² suppressing the global antiferromagnetism and resulting in superconductivity.

Previous low-field^{3–6} and high-field transport studies^{7,8} on different polycrystalline oxypnictides have shown that their magnetotransport behavior is intermediate between conventional low- T_c superconductors and the high-temperature cuprates. However, while LaFeAs(O,F) behaves as an intermediate- T_c superconductor similar to MgB₂ in which thermal fluctuations of vortices do not significantly affect the H - T diagram to the extent that they do in the layered cuprates, the higher- T_c oxypnictides such as SmFeAsO_{0.85} and NdFeAs(O,F) exhibit larger mass anisotropies, enhanced thermal fluctuations, and a Ginzburg parameter comparable to that of YBa₂Cu₃O_{7-x} (YBCO). Thus, the question arises, whether this distinct behavior stems from different critical

temperatures, the presence of magnetic ions,^{9–11} or is due to the electromagnetic granularity of these polycrystalline samples.^{12–14} For example, is the pronounced upward curvature of $H_{c2}(T)$ along the c axis extracted from measurements of the resistivity onsets of polycrystals⁷ indeed an intrinsic feature of $H_{c2}^\perp(T)$ in oxypnictides, or does it reflect an extrinsic effect of magnetic granularity, the onset of the irreversible critical state behavior, and/or melting of the vortex lattice? Moreover, given that the nature of superconductivity in the oxypnictides is still poorly understood, several different scenarios have been proposed in the literature. In particular, many theoretical models are based on the multiband electronic structure of the oxypnictides and on the fact that the superconducting state emerges upon doping of the parent antiferromagnetic semimetal.^{15–19} The multiband effects would manifest themselves in the distinct temperature and orientational dependencies of $H_{c2}(T)$, as has been well documented in detailed studies of MgB₂.^{20–32} To address these issues, we made detailed measurements of the magnetotransport properties of a NdFeAsO_{0.7}F_{0.3} single crystal in very high magnetic fields.

II. SAMPLES

The crystal was made by the flux method using NaCl as the flux. First the starting Nd (purity 99.95%) and As (purity

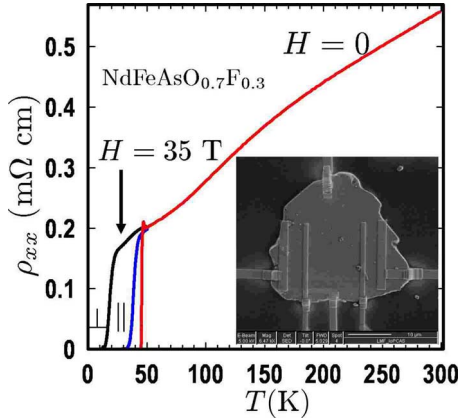


FIG. 1. (Color online) Longitudinal resistivity $\rho_{xx}(T)$ at $H=0$ and 35 T for $H\parallel ab$ and $H\perp ab$. At $B=0$ superconductivity onset is observed at $T_c\approx 46$ K. Inset shows scanning electron micrograph of the sample.

99.99%) were mixed in 1:1 ratio, ground, and pressed into a pellet shape. Then it was sealed in an evacuated quartz tube and reacted at 800 °C for 10 h. The pellet was ground together with a stoichiometric powder mixture of NdF_3 (purity 99.95%), Fe_2O_3 (purity 99.9%), and Fe (purity 99.9%) resulting in $\text{NdFeAsO}_{0.7}\text{F}_{0.3}$ compound. Again it was pressed into a pellet and put together with NaCl powder of mass ratio $\text{NaCl}:\text{NdFeAs}(\text{O},\text{F})=10:1$ and sealed in an evacuated quartz tube and reacted at about 1050 °C for 10 days. Then it was cooled down at a rate of 3 °C/h to 850 °C, followed by a quick cooling to room temperature by shutting off the power of the furnace. The resulting product contains mainly platelike small crystals with lateral dimensions of 5–50 μm and ~ 1 μm thickness.

Previous extensive transport^{33–35} and heat-capacity³⁶ studies on $\text{NdFeAsO}_{0.82}\text{F}_{0.18}$ single crystal revealed the onset of superconductivity at $T_c\approx 47$ K and the upper critical fields $H_{c2}^{\parallel}(0)=304$ T and $H_{c2}^{\perp}(0)=62\text{--}70$ T extrapolated from the Werthamer-Helfand-Hohenberg (WHH) formula.³⁷ These samples also have a relatively small mass anisotropy parameter $\gamma=(m_c/m_a)^{1/2}\leq 5$, where m_a and m_c are the effective masses along the ab plane and the c axis, respectively. However, the above studies were performed in magnetic fields not exceeding 9 T, where most of the multiband effects would not manifest themselves in the $H_{c2}(T)$ curves.

III. RESISTIVE TRANSITIONS AND UPPER CRITICAL FIELDS

For our experiment we used three different high-field magnets at the National High Magnetic Field Laboratory (NHMFL): 35 T dc resistive and 45 T hybrid magnets at Florida State University and 65 T pulsed field magnet at Los Alamos National Laboratory. The inset to Fig. 1(a) shows the scanning electron micrograph of the $\text{NdFeAs}(\text{O},\text{F})$ sample with six Pt contacts fabricated by the focused ion-beam (FIB) technique. The distance between voltage contacts is ~ 13 μm and the sample thickness is ~ 1.4 μm . The sample was glued to a conductive silicon substrate to ensure good

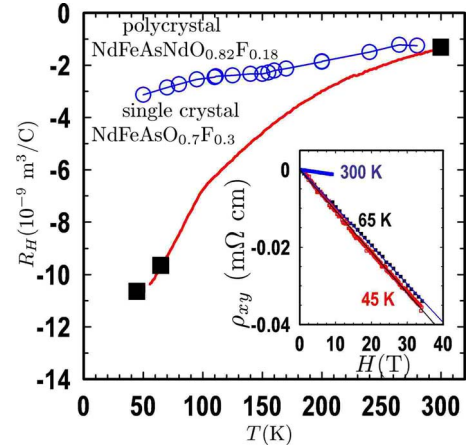


FIG. 2. (Color online) Hall coefficient R_H as a function of T measured in superconducting magnet at ± 9 T (solid line) and determined from linear fits to $\rho_{xy}(H)$ for $-35 < H < 35$ T or $-9 < H < 9$ T (solid squares), as shown in the inset. R_H for polycrystalline $\text{Nd}(\text{O}_{0.94}\text{F}_{0.06})\text{FeA}$ sample is also shown.

thermalization during measurement and to prevent electric charge buildup during the FIB procedure. The sample was placed on a rotating platform, which allows us to change its orientation with respect to the magnetic field *in situ*. The longitudinal resistivity ρ_{xx} and the Hall coefficient R_H in high magnetic fields were measured using a lock-in technique with ac excitation current below 0.3 mA at frequency of 22 Hz. Pulsed field measurements were conducted using in-house synchronous digital lock-in technique at frequency of 16 kHz and similar levels of current.

Figure 1 shows $\rho_{xx}(T)$ as a function of temperature T at $H=0$ and 35 T for different sample orientations. The magnetic field perpendicular to the ab plane shifts the superconducting transitions to lower T , reducing T_c (from 46 to 21 K at $H=35$ T) without significant change in the shape of $\rho_{xx}(T)$. This behavior is reminiscent of magnetotransport in low- T superconductors. In contrast, fields applied parallel to the ab plane change the shape of the resistive transitions more than they do for $H\parallel c$ but less than what was observed on polycrystalline $\text{NdFeAs}(\text{O},\text{F})$.⁸ Figure 1 shows that the $\rho_{xx}(T)$ dependence is sublinear at higher T but superlinear below $T\lesssim 100$ K. Over the same temperature range, the Hall resistivity $\rho_{xy}(T)$ shown in Fig. 2 has a relatively strong temperature dependence for such an optimally doped material. This dependence is much stronger than was observed on a polycrystalline sample with much lower doping, $x=6\%$,⁸ with $\rho_{xy}(T)$ exhibiting a kink around $T\approx 100$ K. Such temperature dependencies of the transport coefficients near ~ 100 K may result from a multiband conductivity or a structural transition. The inset to Fig. 2 shows $\rho_{xy}(H)$ at selected temperatures. On this field scale, $\rho_{xy}(H)$ does not exhibit field nonlinearities, at $40 < T < 300$ K, similarly to polycrystalline samples.⁸ However, a strong dependence of $R_H(H)$ is observed in this single crystal at lower temperatures as will be discussed later.

Figures 3–6 show the detailed field and temperature dependencies of $\rho_{xx}(T, H)$, from which the upper critical fields parallel and perpendicular to the ab planes were extracted.

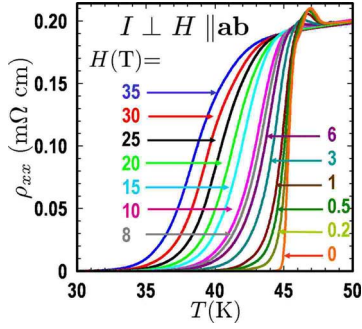


FIG. 3. (Color online) ρ_{xx} as a function of temperature at various magnetic fields for $H \parallel ab$.

Here, H_{c2} for both field orientations was measured at the onset of the superconductivity transition defined by the intersection point from linear extrapolations of $\rho_{xx}(T, H)$ at $T < T_c$ and $\rho_n(T, H)$ at $T > T_c$, as shown in Fig. 4. Here, $\rho_n(T, H)$ is the resistivity in the normal state. We also extracted the midtransition field $H_{50}(T)$ and the resistivity onset fields $H_{10}(T)$ and $H_{0.5}(T)$ defined by $\rho_{xx}(T, H) = 0.5\rho_n(T, H)$, $0.1\rho_n(T, H)$, and $0.05\rho_n(T, H)$, respectively. The fields $H_{0.5}(T)$ are close to the irreversibility field H^* , which quantifies the onset of vortex critical state. The resulting temperature dependencies of all these fields are summarized in Figs. 8 and 9. Notice that the $R(T)$ curves shown in Figs. 3–6 exhibit a small peak just before the transition which disappears at $H > 4$ T for $H \parallel c$ and $H > 6$ T for $H \parallel ab$. Such resistance peak anomaly has been observed in other superconductors and is usually ascribed to the effect of paramagnetic ions, sample inhomogeneities, contact arrangements, etc.^{38–41} Since the mechanism of this anomaly is still not completely understood, we did not take it into account when extracting H_{c2} from the data shown in Figs. 3–6.

Figure 7(a) shows the magnetoresistance (MR) at $T = 50$ K, just above the onset of superconductivity. The MR is positive for $H \parallel c$ and negative for $H \parallel ab$. The difference could be attributed to orbital origin of this MR. As shown in Fig. 7(b), the magnetoresistance $[\rho_{xx}(H) - \rho_{xx}(0)] / \rho_{xx}(0) \propto H^2$ for both field orientations and $H \gtrsim 15$ T exhibits a quadratic field dependence. However, if this quadratic contributions are removed, a weak remanent positive MR is observed

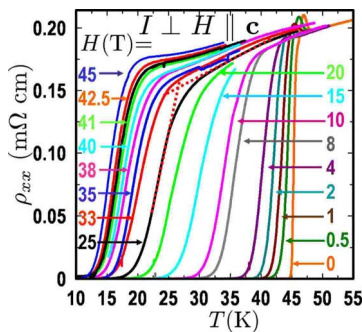


FIG. 4. (Color online) ρ_{xx} as a function of temperature at various magnetic fields for $H \perp ab$. Dotted lines show how the onset of the transition was determined for $H = 20$ T. Excitation current $I \leq 0.3$ mA at frequency $f = 22$ Hz was applied in the ab plane.

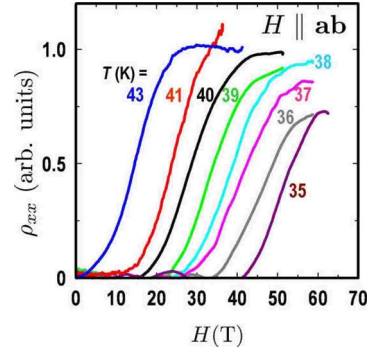


FIG. 5. (Color online) The longitudinal resistivity $\rho_{xx}(H)$ as a function of magnetic field in for $H \parallel ab$ measured in pulsed magnet up to 60 T.

at low fields $H \leq 15$ T, as shown in Fig. 7(c). This remanent MR is identical for both field orientations, which in turn suggests a spin mechanism behind this positive MR component. Interestingly, such a spin-dependent positive MR is ubiquitous in diluted magnetic semiconductors (DMSs) in the paramagnetic phase.^{42–44} It originates from the giant spin splitting Δ_s of the electron states, which considerably affects quantum corrections to the conductivity brought about by the effect of disorder-modified electron-electron interactions.⁴⁵ Since Δ_s in DMSs is proportional to the magnetization M of the localized spins, this positive MR scales with B and T like the Brillouin function. Importantly, this positive MR is absent in a ferromagnetic phase when localized moments are already aligned at $H = 0$. This mechanism can also produce MR in NdFeAs(O,F) provided that at least some of localized magnetic moments μ (most likely of Nd^{3+} ions with $\mu = 3.6\mu_B$) are in a paramagnetic phase. At the same time, as shown in Fig. 7(d), the Hall coefficient R_H strongly depends on H at low field. Such a dependence could result not only from quantum corrections to ρ_{xy} from electron-electron interactions, but it may also be a result of multiband conductivity as well.

Based on the results shown in Figs. 8 and 9, the following points can be made:

- (1) The 100–200 T field scale of H_{c2} in $\text{NdFeAsO}_{0.7}\text{F}_{0.3}$ is comparable to that of high- T_c cuprates.
- (2) $H_{c2}^\perp(T)$ perpendicular to the ab plane exhibits a pronounced upward curvature similar to what was first reported

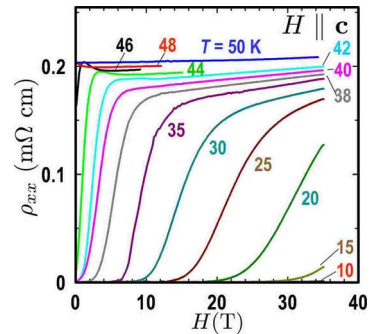


FIG. 6. (Color online) The longitudinal resistivity $\rho_{xx}(H)$ as a function of magnetic field in for $H \perp ab$ measured in dc resistive magnet up to 35 T at various temperatures.

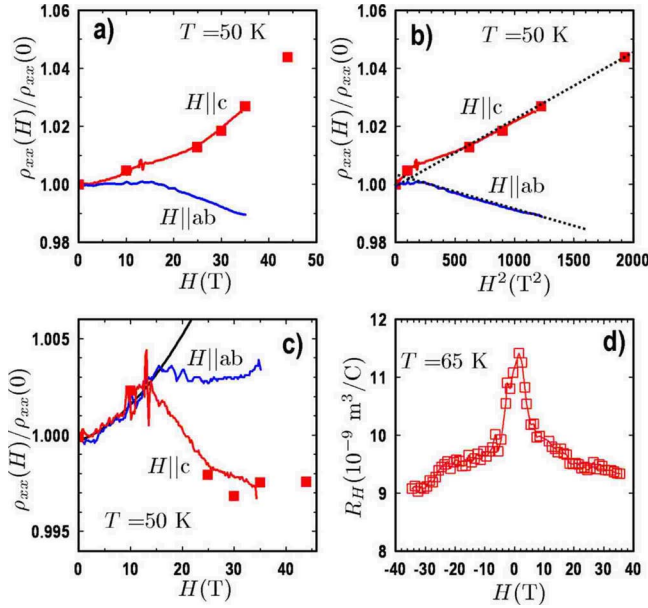


FIG. 7. (Color online) Magnetoresistance measured at $T = 50$ K for two different sample configurations. Squares denote data from temperature sweeps at fixed magnetic field, while solid lines were measured at fixed T . (b) The same data plotted versus H^2 . Dotted lines show linear fits taken for $H \geq 15$ T. (c) Data plotted after subtraction of the H^2 contribution. (d) Hall coefficient $R_H(H) = \rho_{xy}(H)/H$ versus magnetic field measured at $T = 65$ K.

for polycrystalline LaFeAs(O,F).⁷ This is very different from the one-band WHH behavior and appears to be an intrinsic property of oxypnictides rather than manifestations of the vortex melting or the onset of pinning at $H = H^*(T)$.

(3) The slopes $H'_{c2}^{\parallel} = |dH_{c2}^{\parallel}/dT|$ and $H'_{c2}^{\perp} = |dH_{c2}^{\perp}/dT|$ for both field orientations increase significantly just a few kelvins below T_c . Thus, low-field $H < 9$ T measurements may underestimate the actual values of $H'_{c2}^{\perp} = \phi_0/2\pi\xi_{a0}^2T_c$ and $H'_{c2}^{\parallel} = \phi_0/2\pi\xi_{a0}\xi_{c0}T_c$ at $T \approx T_c$, from which the coherence

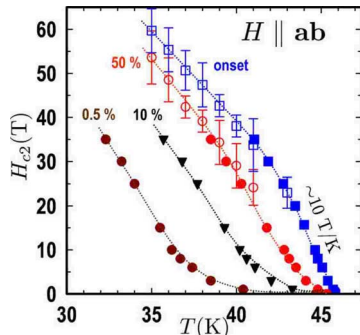


FIG. 8. (Color online) Temperature dependence of the upper critical field $H_{c2}^{\parallel}(T)$ along the ab plane obtained from dc (filled symbols) and pulsed (open symbols) measurements. The data extracted from the results shown in Figs. 3 and 5 show the temperatures at which the resistance reaches 0.5%, 10%, and 50% of the normal-state resistance, as extrapolated linearly from the $\rho_N(T,H)$ temperature dependence above $T_c(H)$. The onsets of superconducting transition were determined as shown in Fig. 4 and corresponded well to the 90% transitions. The dotted lines are guides to the eyes.

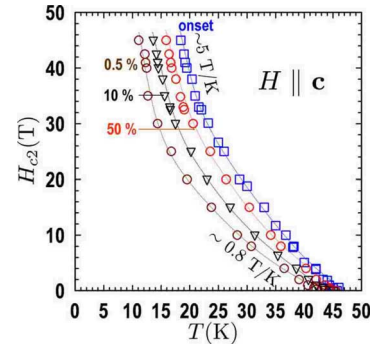


FIG. 9. (Color online) Temperature dependence of the upper critical fields $H_{c2}^{\perp}(T)$ along the c axis obtained from the dc measurements. The data extracted from the results shown in Figs. 4 and 6 show the temperatures at which the resistance reaches 0.5%, 10%, and 50% of the normal-state resistance, as extrapolated linearly from the $\rho_N(T,H)$ temperature dependence above $T_c(H)$. The onsets of superconducting transition were determined as shown in Fig. 4 and corresponded well to the 90% transitions. The dashed lines are guides to the eyes.

lengths $\xi_a(T) = (1 - T/T_c)^{-1/2}\xi_{a0}$ and $\xi_c(T) = (1 - T/T_c)^{-1/2}\xi_{c0}$ in the ab plane and along the c axis can be extracted. As it is evident from Figs. 8 and 9, the high-temperature slopes H'_{c2}^{\perp} and H'_{c2}^{\parallel} attain different values above ≈ 10 T, so the use of high magnetic fields becomes decisive for revealing the true intrinsic superconducting parameters of NdFeAsO_{0.7}F_{0.3} single crystals. This may also explain why low-field measurements^{33–35} show lower values of dH_{c2}^{\parallel}/dT and dH_{c2}^{\perp}/dT .

IV. THERMALLY-ACTIVATED RESISTIVITY

Shown in Figs. 10 and 11 are the temperature dependencies of the Ohmic resistivity $\rho_{xx}(T,H)$ measured above the irreversibility field $H^* < H < H_{c2}$ for both field orientations. These data can be described well by the Arrhenius dependence

$$\ln \rho_{xx} = \ln \rho_0 - E_a(T,H)/T, \quad (1)$$

which is a characteristic of thermally-activated flux flow (TAFF) of vortices and has been studied extensively on high- T_c cuprates. Here, $E_a(T,B) = -\partial \ln \rho_{xx} / \partial (1/T)$ is the ac-

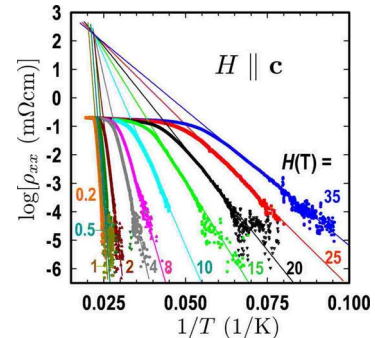


FIG. 10. (Color online) Arrhenius plot for $\rho_{xx}(T)$ at different magnetic fields perpendicular to the ab plane.

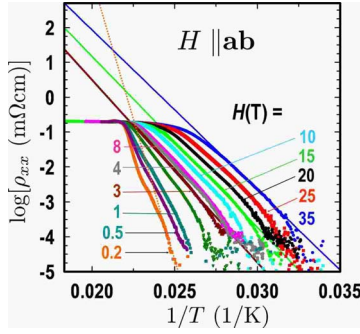


FIG. 11. (Color online) Arrhenius plot for $\rho_{xx}(T)$ at different magnetic fields parallel to the ab plane.

tivation energy determined by hopping of vortex bundles in the pinning potential. Several features of the data shown in Figs. 10 and 11 should be pointed out.

(1) The Arrhenius dependence holds over 4–5 decades of ρ_{xx} down to the limit of sensitivity of our transport measurements. This indicates that thermally-activated vortex hopping in $\text{NdFeAsO}_{0.7}\text{F}_{0.3}$ is similar to that of high- T_c cuprates and is much more pronounced than in lower- T_c pnictides such as $\text{LaFeAsO}_{1-x}\text{F}_x$. The good linear behavior evident from Figs. 10 and 11 also indicates that the low-temperature dependence of $E_a(T)$ is approximately linear, $E_a(T) = E_m(1 - T/T_m)$, where T_m is a parameter with the dimensionality of temperature. In this case the term T/T_m can be eliminated by redefining $\rho_0 \rightarrow \rho_0 \exp(E_m/T_m)$ in Eq. (1) without changing any observed characteristics.

(2) The higher-temperature $\log \rho_{xx}(T)$ data level off at a field-independent value corresponding to the normal-state resistivity ρ_n .

(3) The $\log \rho_{xx}(T)$ lines for different $H \parallel c$ extrapolate to the same temperature $\approx T_c$, indicating that $T_m = T_c$, $\rho_0 \approx \rho_n \exp(E_m/T_c)$, and E_m is practically independent of H . However, for the parallel field orientation, this is not the case because of the field dependence of E_m , as shown below.

From the low-temperature slope of $\log \rho_{xx}$ the field dependencies of the activation energy $E_a = -d \ln \rho_{xx} / d(1/T)$ can be obtained. The results presented in Fig. 12 for both field orientations show that $E_a \approx (3-4) \times 10^3$ K at low fields. The activation energy $E_a \approx 2 \times 10^4$ K for a polycrystalline NdFeAs(O,F) measured previously⁸ is higher than for the single

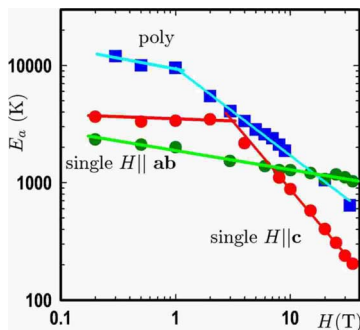


FIG. 12. (Color online) Field dependencies of the activation energy $E_a(H)$ for $H \perp ab$ and $H \parallel ab$. The solid squares show the data for NdFeAs(O,F) polycrystal measured earlier.

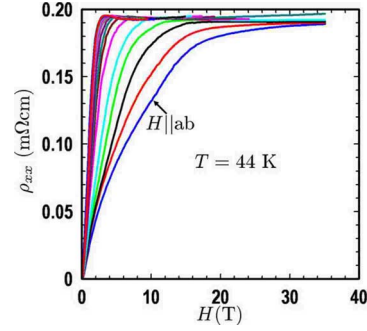


FIG. 13. (Color online) The resistivities $\rho_{xx}(T, H)$ measured at 44 K for different angles θ between \mathbf{H} and the ab plane.

crystals studied in this work [similar thermally-activated resistivity was recently observed on polycrystalline $\text{NdFeAsO}_{0.82}\text{F}_{0.18}$ (Ref. 6)]. The field dependencies of $E_a(B)$ for $H \parallel c$ and $H \perp c$ are also markedly different. $E_a(H)$ for $H \parallel c$ exhibits a rather conventional field dependence characteristic of thermally-activated transport: a constant value at low fields $H < 3$ T, where single-vortex pinning dominates, followed by a power-law decrease $E_m \propto H^{-1.1}$ characteristic of collective creep at higher fields $H > 3$ T.⁴⁶ By contrast, the activation energy for $H \parallel ab$ exhibits a rather weak power-law decrease $E_m \propto H^{-0.17}$ in the entire field interval where $\rho_{xx}(T, H)$ was measured.

The field and temperature dependencies of $E_a(T, H)$ can be described by the following scaling function:

$$E_a = \frac{E_0(1 - T/T_c)^\alpha}{[1 + H/H_0(T)]^\beta} \left[1 - \frac{H}{H_{c2}(T)} \right]^\delta, \quad (2)$$

where H_0 quantifies the field above which vortex dynamics is determined by collective effects of vortex interaction.⁴⁶ From the data presented above, we obtain $H_0 \approx 3$ T, $\alpha \approx 1$, and $\beta \approx 1.1$ for $H \parallel c$ and $\beta \approx 0.17$ for $H \parallel ab$.

V. ANGULAR DEPENDENCIES

The TAFF resistivity $\rho_{xx}(T, H, \theta)$ was measured at different angles θ between \mathbf{H} and the ab plane, as illustrated by a representative example shown in Fig. 13. The angular dependencies of $H_{c2}(\theta)$ extracted from $\rho_{xx}(T, H, \theta)$ at 90%, 50%, and 10% of $\rho_n(T, H)$ are shown in Fig. 14.

It is clearly seen that the anisotropy as $\gamma = H_{c2}^{\parallel} / H_{c2}^{\perp}$ decreases when calculated at lower ρ_{xx} . At the same time $H_{c2}^{90\%}(\theta)$ shown in Fig. 14 notably departs from the standard Ginzburg-Landau (GL) formula

$$H_{c2}(\theta) = \frac{H_{c2}^{\perp}}{\sqrt{\sin^2 \theta + \gamma^{-2} \cos^2 \theta}}, \quad (3)$$

where $\gamma = (m_c/m_a)^{1/2}$ is defined by the ratio of effective masses along the ab plane and the c axis. The fit to Eq. (3) yields $\gamma \approx 8.9$ in this case. Data taken at 50% and 10% departure from Eq. (3) even stronger, which may result from increasing contribution of TAFF transport at lower resistivities.

The temperature dependencies of $\gamma(T)$ obtained from the H_{c2} data shown in Figs. 8 and 9 for H_{10} , H_{50} , and H_{c2} are

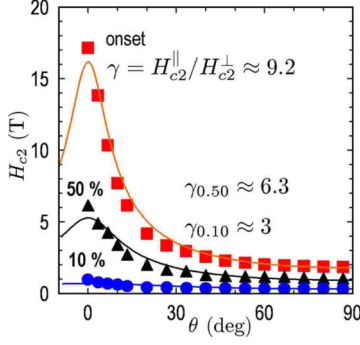


FIG. 14. (Color online) Angular dependence of $H_{c2}(\theta)$ defined at $\rho_{xx} = (0.9, 0.5, 0.1)\rho_n$ at 44 K. The solid lines show the fits with Eq. (3).

shown in Fig. 15. Contrary to the standard one-band behavior, γ turns out to be temperature dependent, with the values of $\gamma_{10}(T)$, $\gamma_{50}(T)$, and $\gamma(T)$ being rather different especially just below T_c . While the parameter of H_{c2} anisotropy $\gamma(T) = H_{c2}^{\parallel}/H_{c2}^{\perp}$ decreases from ≈ 9 at T_c to ≈ 5 at 34 K, the field H_{10} becomes more anisotropic upon decreasing T . Below $T \approx 38$ K, however, these values of $\gamma(T)$ converge.

VI. H_{c2} IN TWO-BAND SUPERCONDUCTORS

We interpret our experimental data using a generic two-band BCS model, which enables us to address the constraints imposed by the observed shapes of $H_{c2}(T)$ on different multi-band pairing models suggested in the literature. For negligible interband impurity scattering, T_c is given by^{47,48}

$$T_{c0} = \Omega \exp[-(\lambda_+ - s\lambda_0)/2w], \quad (4)$$

where $\lambda_{\pm} = \lambda_{11} \pm \lambda_{22}$, $w = \lambda_{11}\lambda_{22} - \lambda_{12}\lambda_{21}$, $s = \text{sign}(w)$, and $\lambda_0 = (\lambda_{-}^2 + 4\lambda_{12}\lambda_{21})^{1/2}$; λ_{12} and λ_{22} are pairing constants in bands 1 and 2; and λ_{12} and λ_{21} quantify interband coupling. Since the microscopic pairing mechanisms in oxypnictides are not well understood, the matrix λ_{ij} is treated here phenomenologically, but the main results turn out to be not very sensitive to the particular choice of λ_{ij} . For s -wave pairing, intraband impurity scattering does not affect T_{c0} , while weak interband scattering reduces T_c according to^{26,49,50}

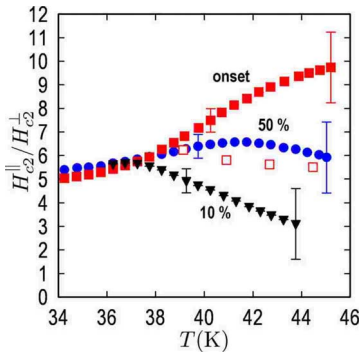


FIG. 15. (Color online) Temperature dependencies of γ_{10} , γ_{50} , and γ_{90} . The open squares show the data from Ref. 35 measured on NdFeAsO_{0.82}F_{0.18} single crystal with higher $T_c = 51.5$ K. These data are plotted at reduced temperatures.

$$T_c = T_{c0} - \frac{\pi}{8\lambda_0} [\lambda_0 \gamma_+ + \lambda_- \gamma_- - 2\lambda_{21} \gamma_{12} - 2\lambda_{12} \gamma_{21}], \quad (5)$$

where $\gamma_{\pm} = \gamma_{12} \pm \gamma_{21}$ and γ_{12} and γ_{21} are scattering rates between bands 1 and 2; $N_1 \gamma_{12} = N_2 \gamma_{21}$ and $N_1 \lambda_{12} = N_2 \lambda_{21}$, where N_1 and N_2 are partial densities of states in bands 1 and 2, respectively. In the following, we discuss two scenarios: (1) conventional s -wave pairing dominated by strong intraband coupling $w > 0$ and (2) strong interband pairing $w < 0$ which can result in the π shift between the order parameters on two bands for interband repulsion $\lambda_{12} < 0$ (s^{\pm} pairing¹⁵).

As follows from Eq. (5), interband repulsion with $\lambda_{12} < 0$ and $\lambda_{21} < 0$ enhances T_c depression due to interband scattering between different pieces of the Fermi surface with the opposite signs of the order parameter. This suppression may be reduced by strong-coupling effects.⁵¹ By contrast, for strong interband attraction $4\lambda_{12}\lambda_{21} \gg \lambda_{-}^2$, Eq. (5) yields

$$T_c = T_{c0} - \frac{\pi \gamma_{12}}{8} \left(1 - \sqrt{\frac{N_1}{N_2}} \right)^2. \quad (6)$$

Here, T_c suppression is much weaker than for the s^{\pm} pairing due to the factor $(1 - \sqrt{N_1/N_2})^2$, which makes T_c independent of γ_{12} in the special case of $N_1 = N_2$.

In the dirty limit, the equation for H_{c2} , which takes into account both orbital and Zeeman pair breaking for negligible interband scattering, can be written in the following parametric form:²⁶

$$\ln t = -[U_1(h) + U_2(h) + \lambda_0/w]/2 + s\{[U_1(h) - U_2(h) - \lambda_-/w]^2/4 + \lambda_{12}\lambda_{21}/w^2\}^{1/2}, \quad (7)$$

$$H_{c2} = 2\phi_0 k_B T_c t h / \hbar D_0, \quad (8)$$

$$U_{1,2}(h) = \text{Re } \psi[1/2 + (i + D_{1,2}/D_0)h] - \psi(1/2), \quad (9)$$

where $t = T/T_{c0}$, $\psi(x)$ is the digamma function, $\eta = D_2/D_1$, D_1 and D_2 are diffusivities in band 1 and 2, $D_0 = \hbar/2m$, and the parameter h runs from 0 to ∞ as T varies from T_c to 0. For $D_1 = D_2$ and negligible Zeeman pair breaking $D_0 \ll D_{1,2}$, Eq. (8) simplifies to the one-band de-Gennes-Maki equation $\ln t + U(h) = 0$. If the magnetic field \mathbf{H} is inclined by the angle θ with respect to the ab planes, Eqs. (8) and (9) also describe the angular dependence of $H_{c2}(\theta)$ if $D_{1,2}$ are replaced by their angular-dependent values

$$D_m(\theta) = [D_m^{(a)2} \sin^2 \theta + D_m^{(a)} D_m^{(c)} \cos^2 \theta]^{1/2}, \quad (10)$$

where $m = 1, 2$ and $D_m^{(a)}$ and $D_m^{(c)}$ are the in-plane and the c -axis principal values of $D_m^{\alpha\beta}$.

$H_{c2}(T)$ curves shown in Figs. 8 and 9 exhibit pronounced upward curvature for $H_{\parallel}c$ and the downward curvature for $H_{\perp}c$ similar to the behavior of $H_{c2}(T)$ first observed on polycrystalline LaFeAsO_{0.89}F_{0.11}.⁷ Such temperature dependence of $H_{c2}(T)$ has been often observed on MgB₂, suggesting that the two-band theory with $D_1 \neq D_2$ could also be used to describe $H_{c2}(T)$ in oxypnictides (the superconducting gaps on the disconnected pieces of the Fermi surface can be either different or the same). If interband scattering is negligible, neither T_c nor H_{c2} depend on the sign of λ_{12} , so we consider two different cases: (1) dominant intraband coupling w

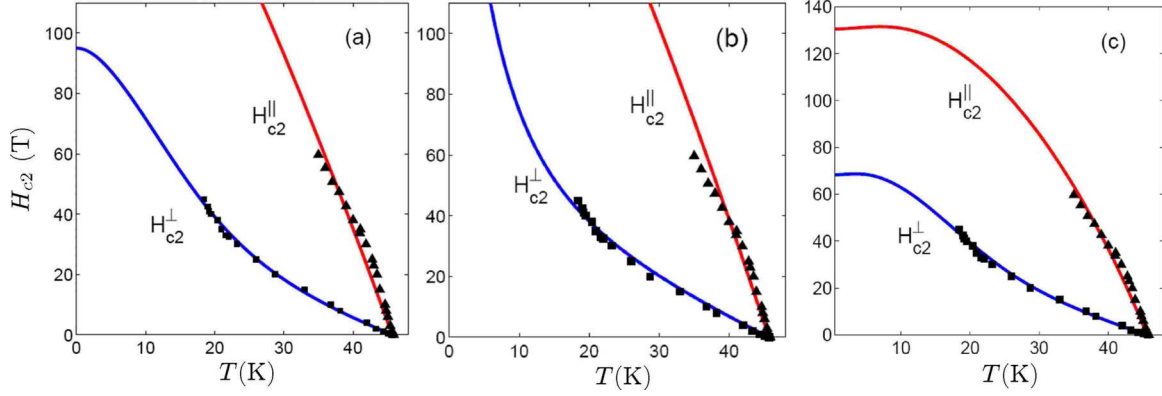


FIG. 16. (Color online) Fits of Eqs. (8) and (9) to the experimental data shown in Figs. 8 and 9 for different pairing scenarios: (a) $w > 0$, $\lambda_{11}=\lambda_{22}=0.5$, $\lambda_{12}=\lambda_{21}=0.25$, $\eta_{\perp}=D_2^{(a)}/D_1^{(b)}=0.08$, $\eta_{\parallel}=[D_2^{(a)}D_2^{(c)}/D_1^{(a)}D_1^{(c)}]^{1/2}=1$, and negligible paramagnetic effects; (b) $w < 0$, $\lambda_{11}=\lambda_{22}=0.49$, $\lambda_{12}=\lambda_{21}=0.5$, $\eta_{\perp}=D_2^{(a)}/D_1^{(b)}=0.007$, $\eta_{\parallel}=[D_2^{(a)}D_2^{(c)}/D_1^{(a)}D_1^{(c)}]^{1/2}=1$, and negligible paramagnetic effects; and (c) $w > 0$, $\lambda_{11}=\lambda_{22}=0.5$, $\lambda_{12}=\lambda_{21}=0.25$, $\eta_{\perp}=D_2^{(a)}/D_1^{(b)}=0.08$, $\eta_{\parallel}=[D_2^{(a)}D_2^{(c)}/D_1^{(a)}D_1^{(c)}]^{1/2}=1$, $d_{\perp}=D_1^{(a)}/D_0=10$, and $d_{\parallel}=[D_2^{(a)}D_2^{(c)}/D_1^{(a)}D_1^{(c)}]^{1/2}/D_0=0.7$.

$=\lambda_{11}\lambda_{22}-\lambda_{12}\lambda_{21} > 0$ and (2) dominant interband coupling $w = \lambda_{11}\lambda_{22}-\lambda_{12}\lambda_{21} < 0$.

Shown in Fig. 16(a) is an example of the fit of Eqs. (8) and (9) to the data for $\lambda_{11}=\lambda_{22}=0.5$ and $\lambda_{12}=\lambda_{21}=0.25$, in which case $T_c = \Omega \exp[-1/(\lambda_{11}+\lambda_{12})] = 50$ K corresponds to $\Omega \approx 190$ K. Figure 16(a) shows the fit without taking paramagnetic effects into account for $D_2=0.08D_1$, which suggests that the electron mobility in one band is different from that in the other. We do not discuss here microscopic mechanisms responsible for such band disparity and the particular values of λ_{mn} ; instead, we focus on the set of parameters which fit the data and the extent to which these parameters are different for the cases of $w > 0$ and $w < 0$. Extrapolations of $H_{c2}^{\parallel}(T)$ to $T=0$ based on the observed slope at T_c suggests that $H_{c2}^{\parallel}(0) \sim 220$ T, which is well above the weak-coupling BCS paramagnetic limit $H_p[T] = 1.84T_c[K] \approx 90$ T.

Figure 16(b) shows the fit in the case of strong interband pairing $\lambda_{12}\lambda_{21} > \lambda_{11}\lambda_{21}$ for $\lambda_{11}=\lambda_{22}=0.49$, $\lambda_{12}=\lambda_{21}=0.5$, and $D_2^a=0.007D_1^a$. Reproducing the observed upward curvature of $H_{c2}^{\perp}(T)$ for this case requires a much greater difference of the band diffusivities than for the previous case. Reducing λ_{11} and λ_{22} shifts the region of upward curvature to lower temperatures, which makes fitting the data even more difficult.

Given the very high extrapolated values of $H_{c2}^{\parallel}(0)$ in Fig. 16(a), the role of paramagnetic effects becomes important. Shown in Fig. 16(c) is the fit for the same parameters as in Fig. 16(a) but with the account of the Zeeman pair breaking for $D_1^{(a)}=10D_0$ and $[D_2^{(a)}D_2^{(c)}/D_1^{(a)}D_1^{(c)}]^{1/2}=0.7D_0$. In this case, the values of $H_{c2}(T)$ at low temperatures are significantly reduced as compared to what may be expected from the fit in Fig. 16(a), which ignores the paramagnetic effects.

Several points should be made regarding the fits in Figs. 16(a)–16(c). First, applying BCS weak couplings Eqs. (8) and (9) to a superconductor with $T_c=50$ K neglects the strong-coupling renormalization effects of the Eliashberg theory. However, given the lack of microscopic theory of superconductivity in oxypnictides, our qualitative analysis based on the BCS model may be justified since the shapes of $H_{c2}(T)$ described by Eqs. (8) and (9) mostly depend on the ratio D_2/D_1 but are rather weakly sensitive to the particular choice of the coupling constants. A conventional way of

treating strong-coupling effects is to express Eqs. (8) and (9) in terms of experimentally observed parameters⁵² such as T_c and D_1 and D_2 extracted from normal-state transport measurements and the observed slopes dH_{c2}/dT . The use of the dirty limit is not crucial since the upward curvature of $H_{c2}(T)$ generally requires a significant band asymmetry in the two-band clean limit as well.⁵³ Another point is that the actual paramagnetic limit $H_p \approx (1+\lambda)H_p^{\text{BCS}}$ is significantly enhanced by strong-coupling effects as compared to the BCS value.⁵⁴ Here, $\lambda \sim 1$ is a characteristic bare coupling constant for the exchange boson, so $H_{c2}(T)$ values may significantly exceed H_p^{BCS} as has been observed in other superconductors, for example, PbMo_6S_8 .^{55,56} Thus, Eqs. (8) and (9) may capture the qualitative behavior of $H_{c2}(T)$ as a function of materials parameters if they are expressed in terms of the observed quantities and if the Zeeman terms are renormalized by strong-coupling effects.

VII. DISCUSSION

Our high-field data obtained on a $\text{NdFeAsO}_{1-x}\text{F}_x$ single crystals show extremely high H_{c2} values, consistent with previous low-field measurements on single crystals^{3,33–36} and high-field measurements on polycrystals.^{7,8} Our values of the temperature-dependent H_{c2} slopes $H_{c2}^{\parallel} \approx 8\text{--}10$ T/K and $H_{c2}^{\perp} \approx 1.2\text{--}5$ T/K measured from the resistivity onset of superconductivity are considerably higher than the values of H_{c2} extracted from calorimetry measurements on $\text{NdFeAsO}_{1-x}\text{F}_x$ single crystals,³⁶ which may be affected by strong paramagnetism of Nd^{3+} ions at high fields.¹⁰ We should also mention several issues, which may complicate accurate extraction of the anisotropy in $\text{NdFeAsO}_{1-x}\text{F}_x$ single crystals grown by the flux method, which usually results in intergrowths and stacking faults parallel to the ab plane. Such planar defects may increase the apparent anisotropy parameter γ and give rise to the local modulations of order parameter along the c axis. The latter may broaden the resistive transition at T_c and the upward curvature of $H_{c2}(T)$ near T_c , which could mask the two-band effects.

Because of very high values of H_{c2}^{\parallel} and H_{c2}^{\perp} , our high-field measurements up to 60 T are still mostly limited to the

temperatures not too far from T_c , particularly for the field parallel to the ab plane. As a result, it is hard to unambiguously evaluate the values $H_{c2}(0)$, as Figs. 16(a)–16(c) illustrate. Yet, we can evaluate the in-plane and the c -axis GL coherence lengths $\xi_a = (\phi_0/2\pi H'_{c2} T_c)^{1/2} \approx 2.3$ nm and $\xi_c = \xi_a/\gamma = 0.26$ nm for $\gamma=9$, $H'_{c2\perp} = 1.2$ T/K, and $T_c = 50$ K. These values of ξ_a and ξ_c are not too different from those for $\text{YBa}_2\text{Cu}_3\text{O}_{7-x}$. The fits shown in Figs. 16(a)–16(c) also indicate the importance of paramagnetic effects in $H_{c2}(T)$, particularly the fact that extrapolations of H_{c2} to low temperatures based on the measured slope H'_{c2} and the WHH dirty limit formula $H_{c2} \approx 0.7T_c H'_{c2}$ (Ref. 5) may grossly overestimate $H_{c2}(0)$. At the same time, the importance of paramagnetic effects in oxypnictides might open up possibilities of observing first-order phase transitions or perhaps the Fulde-Ferrel-Larkin-Ovchinnikov inhomogeneous states at very high magnetic fields.

The temperature dependence of $H_{c2}^{\perp}(T)$ shown in Fig. 9 is rather different from the conventional one-band WHH behavior, which may be characteristic of many oxypnictides. This confirms our earlier qualitative conclusion inferred from indirect measurements of $H_{c2}^{\perp}(T)$ on polycrystalline oxypnictides.⁷ One possibility to explain the significant upward curvature of $H_{c2}^{\perp}(T)$ is based on the two-band model. This conclusion is also consistent with the temperature-dependent mass anisotropy parameter $\gamma(T)$ reminiscent of the behavior of MgB_2 .^{26,57} Yet, many important points remain controversial. First, to explain the observed upward curvature of $H_{c2}^{\perp}(T)$, we had to assume a rather high difference in the intraband diffusivities $D_2 \sim (0.1-0.01)D_1$ (depending on the pairing scenario) considerably higher than the effective-mass difference for Γ and M electron pockets predicted by *ab initio* calculations.¹⁶⁻¹⁹ One, therefore, has to assume that scattering on impurities or strong magnetic excitations may produce such big differences in D_1 and D_2 .

Our data enable us to make further qualitative conclusions regarding the s -wave two-band pairing scenarios with and without the interband π shift. The first one is less susceptible to the pair-breaking effect of interband impurity scattering, as follows from Eqs. (5) and (6). Indeed, the fact that our $\text{NdFeAs}(\text{O},\text{F})$ single crystal has the same T_c as sintered multiphase polycrystals seems to suggest that the impurity scattering does not suppress T_c much. The latter may also indicate that oxypnictides are effectively in the clean limit just because of their short coherence lengths $\xi_a < \ell$, where ℓ is

the mean-free path. Yet, s^{\pm} pairing is certainly more susceptible to the pair-breaking interband impurity scattering. Another indication that the s -wave pairing without the interband π shift appears to fit our data better comes from the fact that, in order to explain the observed upward curvature of $H_{c2}^{\perp}(T)$ in Fig. 16(b) in the s^{\pm} model, we have to assume the ratio D_1/D_2 to be about an order of magnitude smaller than $D_2/D_1 \sim 0.1$ required for the model of strong intraband pairing and weaker interband pairing.

As far as vortex dynamics in $\text{NbFeAs}(\text{O},\text{F})$ is concerned, our data presented in Figs. 3 and 4 show that high magnetic fields parallel to the c axis mostly shift the resistive transition without significant broadening of the $\rho_{xx}(T)$ curves, while H parallel to the ab plane changes the shape of $\rho_{xx}(T)$ but certainly not as strong as for high- T_c cuprates.⁴⁶ This suggests that, despite the rather high values of γ , thermal fluctuation of vortices in $\text{NbFeAs}(\text{O},\text{F})$ single crystals are weaker than in most anisotropic layered cuprates such as Bi-2212 . This conclusion is consistent with the data of other groups⁵⁸ and with the relatively high activation energy $E_0 \sim 3 \times 10^3$ K extracted from our transport measurements. The effect of thermal fluctuations is also quantified by the Ginzburg parameter $\text{Gi} = (2\pi k_B T_c \mu_0 \Lambda_0^2 / \phi_0^2 \xi_c^2)^{1/2}$, where Λ_0 is the in-plane London penetration depth. Taking $\Lambda_0 = 200$ nm, $\xi_c = 0.26$ nm, and $T_c = 49$ K, we obtain $\text{Gi} \approx 10^{-2}$, which is of the order of the typical Ginzburg number for YBCO. For two-band superconductors, the above estimates of Gi remain qualitatively the same if γ and ξ are taken for the band with the minimum effective mass or maximum electron mobility.²⁶ By contrast, Gi in $\text{LaFeAs}(\text{O},\text{F})$ is close to Gi in MgB_2 , about 30 times smaller than Gi in $\text{NdFeAs}(\text{O},\text{F})$.^{7,8}

In conclusion, our high-field magnetotransport measurements on single-crystal $\text{NdFeAsO}_{0.70}\text{F}_{0.30}$ have revealed very high upper critical fields and their anomalous temperature dependencies. We also observe a pronounced thermally-activated flux flow resistivity which may indicate rich vortex dynamics in single-layer oxypnictides.

ACKNOWLEDGMENTS

The work at NHMFL was supported by the NSF under Cooperative Agreement No. DMR-0084173, by the State of Florida, by the DOE, by the NHMFL IHRP program (F.H.), and by the AFOSR under Grant No. FA9550-06-1-0474 (A.G. and D.C.L.).

¹Y. Kamihara, T. Watanabe, M. Hirano, and H. Hosono, *J. Am. Chem. Soc.* **130**, 3296 (2008).

²H. Takahashi, K. Igawa, K. Arii, Y. Kamihara, M. Hirano, and H. Hosono, *Nature (London)* **453**, 376 (2008).

³C. Martin *et al.*, arXiv:0807.0876 (unpublished).

⁴J. D. Moore *et al.*, *Supercond. Sci. Technol.* **21**, 092004 (2008).

⁵C. Senatore, R. Flükiger, M. Cantoni, G. Wu, R. H. Liu, and X. H. Chen, *Phys. Rev. B* **78**, 054514 (2008).

⁶X. L. Wang, S. R. Ghorbani, S. X. Dou, X.-L. Shen, W. Yi, Z.-C. Li, and Z.-A. Ren, arXiv:0806.1318 (unpublished).

⁷F. Hunte, J. Jaroszynski, A. Gurevich, D. C. Larbalestier, R. Jin, A. S. Sefat, M. A. McGuire, B. C. Sales, D. K. Christen, and D. Mandrus, *Nature (London)* **453**, 903 (2008).

⁸J. Jaroszynski *et al.*, *Phys. Rev. B* **78**, 064511 (2008).

⁹T. Yildirim, *Phys. Rev. Lett.* **101**, 057010 (2008).

¹⁰C. Tarantini, A. Gurevich, D. C. Larbalestier, Z.-A. Ren, X.-L. Dong, W. Lu, and Z.-X. Zhao, *Phys. Rev. B* **78**, 184501 (2008).

¹¹J. Wu, P. Phillips, and A. H. Castro Neto, *Phys. Rev. Lett.* **101**, 126401 (2008).

¹²A. Yamamoto *et al.*, *Appl. Phys. Lett.* **92**, 252501 (2008).

- ¹³A. Yamamoto *et al.*, *Supercond. Sci. Technol.* **21**, 095008 (2008).
- ¹⁴R. Prozorov, M. E. Tillman, E. D. Mun, and P. C. Canfield, arXiv:0805.2783 (unpublished).
- ¹⁵I. I. Mazin, D. J. Singh, M. D. Johannes, and M. H. Du, *Phys. Rev. Lett.* **101**, 057003 (2008).
- ¹⁶D. J. Singh and M.-H. Du, *Phys. Rev. Lett.* **100**, 237003 (2008).
- ¹⁷S. Raghu, X.-L. Qi, C.-X. Liu, D. J. Scalapino, and S.-C. Zhang, *Phys. Rev. B* **77**, 220503(R) (2008).
- ¹⁸S. Graser, G. R. Boyd, C. Cao, H.-P. Cheng, P. J. Hirschfeld, and D. J. Scalapino, *Phys. Rev. B* **77**, 180514(R) (2008).
- ¹⁹S. Ishibashi, K. Terakura, and H. Hosono, *J. Phys. Soc. Jpn.* **77**, 053709 (2008).
- ²⁰R. H. T. Wilke, S. L. Bud'ko, P. C. Canfield, D. K. Finnemore, R. J. Suplinskas, and S. T. Hannahs, *Phys. Rev. Lett.* **92**, 217003 (2004).
- ²¹L. Lyard, P. Szabó, T. Klein, J. Marcus, C. Marcenat, K. H. Kim, B. W. Kang, H. S. Lee, and S. I. Lee, *Phys. Rev. Lett.* **92**, 057001 (2004).
- ²²A. Rydh *et al.*, *Phys. Rev. B* **70**, 132503 (2004).
- ²³V. Braccini *et al.*, *Phys. Rev. B* **71**, 012504 (2005).
- ²⁴M. Angst, S. L. Bud'ko, R. H. T. Wilke, and P. C. Canfield, *Phys. Rev. B* **71**, 144512 (2005).
- ²⁵H.-J. Kim, H.-S. Lee, B. Kang, W.-H. Yim, Y. Jo, M.-H. Jung, and S.-I. Lee, *Phys. Rev. B* **73**, 064520 (2006).
- ²⁶A. Gurevich, *Physica C* **456**, 160 (2007); *Phys. Rev. B* **67**, 184515 (2003).
- ²⁷S. L. Bud'ko and P. C. Canfield, *Phys. Rev. B* **65**, 212501 (2002); S. L. Bud'ko, P. C. Canfield, and V. G. Kogan, *Physica C* **382**, 85 (2002).
- ²⁸V. Ferrando, P. Manfrinetti, D. Marré, M. Putti, I. Sheikin, C. Tarantini, and C. Ferdeghini, *Phys. Rev. B* **68**, 094517 (2003).
- ²⁹E. Ohmichi, T. Masui, S. Lee, S. Tajima, and T. Osada, *J. Phys. Soc. Jpn.* **73**, 2065 (2004).
- ³⁰A. Gurevich *et al.*, *Supercond. Sci. Technol.* **17**, 278 (2004).
- ³¹A. V. Pogrebnnyakov *et al.*, *Appl. Phys. Lett.* **85**, 2017 (2004).
- ³²P. Samuely, Z. Holanová, S. Budko, and P. Canfield, *Physica C* **435**, 71 (2006).
- ³³Y. Jia, P. Cheng, L. Fang, H. Luo, H. Yang, C. Ren, L. Shan, C. Gu, and H.-H. Wen, *Appl. Phys. Lett.* **93**, 032503 (2008).
- ³⁴P. Cheng, H. Yang, Y. Jia, L. Fang, X. Zhu, G. Mu, and H.-H. Wen, *Phys. Rev. B* **78**, 134508 (2008).
- ³⁵Y. Jia, P. Cheng, L. Fang, H. Yang, C. Ren, L. Shan, C.-Z. Gu, and H.-H. Wen, *Supercond. Sci. Technol.* **21**, 105018 (2008).
- ³⁶U. Welp, R. Xie, A. E. Koshelev, W. K. Kwok, P. Cheng, L. Fang, and H. H. Wen, arXiv:0807.4196 (unpublished).
- ³⁷N. R. Werthamer, E. Helfand, and P. C. Hohenberg, *Phys. Rev.* **147**, 295 (1966).
- ³⁸P. Lindqvist, A. Nordström, and Ö. Rapp, *Phys. Rev. Lett.* **64**, 2941 (1990); A. Nordström and Ö. Rapp, *Phys. Rev. B* **45**, 12577 (1992).
- ³⁹P. Santhanam, C. C. Chi, S. J. Wind, M. J. Brady, and J. J. Bucchignano, *Phys. Rev. Lett.* **66**, 2254 (1991).
- ⁴⁰C. Strunk, V. Bruyndoncx, C. Van Haesendonck, V. V. Moshchalkov, Y. Bruynseraede, C.-J. Chien, B. Burk, and V. Chandrasekhar, *Phys. Rev. B* **57**, 10854 (1998).
- ⁴¹R. Vaglio, C. Attanasio, L. Maritato, and A. Ruosi, *Phys. Rev. B* **47**, 15302 (1993); C. Attanasio, S. Barbenera, T. Di Luccio, S. L. Prischepa, R. Russo, M. Salvato, and L. Maritato, *J. Phys.: Condens. Matter* **13**, 3215 (2001).
- ⁴²M. Sawicki, T. Dietl, J. Kossut, J. Igalson, T. Wojtowicz, and W. Plesiewicz, *Phys. Rev. Lett.* **56**, 508 (1986).
- ⁴³I. P. Smorchkova, N. Samarth, J. M. Kikkawa, and D. D. Awschalom, *Phys. Rev. Lett.* **78**, 3571 (1997).
- ⁴⁴T. Andrearczyk, J. Jaroszyński, G. Grabecki, T. Dietl, T. Fukumura, and M. Kawasaki, *Phys. Rev. B* **72**, 121309(R) (2005).
- ⁴⁵B. L. Al'tshuler and A. G. Aronov, in *Electron-Electron Interactions in Disordered Systems*, edited by A. L. Efros and M. Pollak (North-Holland, Amsterdam, 1985), p. 1; H. Fukuyama, *ibid.*, p. 155; P. A. Lee and T. V. Ramakrishnan, *Rev. Mod. Phys.* **57**, 287 (1985).
- ⁴⁶G. Blatter, M. V. Feigel'man, V. B. Geshkenbein, A. I. Larkin, and V. M. Vinokur, *Rev. Mod. Phys.* **66**, 1125 (1994).
- ⁴⁷H. Suhl, B. T. Matthias, and L. R. Walker, *Phys. Rev. Lett.* **3**, 552 (1959).
- ⁴⁸V. Moskalenko, *Fiz. Met. Metalloved.* **8**, 503 (1959) [*Phys. Met. Metallogr.* **8**, 25 (1959)].
- ⁴⁹A. A. Golubov and I. I. Mazin, *Phys. Rev. B* **55**, 15146 (1997).
- ⁵⁰N. Schopohl and K. Scharnberg, *Solid State Commun.* **22**, 371 (1977).
- ⁵¹Y. Senga and H. Kontani, arXiv:0809.0374 (unpublished).
- ⁵²J. A. X. Alexander, T. P. Orlando, D. Rainer, and P. M. Tedrow, *Phys. Rev. B* **31**, 5811 (1985).
- ⁵³T. Dahm and N. Schopohl, *Phys. Rev. Lett.* **91**, 017001 (2003).
- ⁵⁴M. Schossmann and J. P. Carbotte, *Phys. Rev. B* **39**, 4210 (1989).
- ⁵⁵Ø. Fischer, *Appl. Phys.* **16**, 1 (1978).
- ⁵⁶H. J. Niu and D. P. Hampshire, *Phys. Rev. B* **69**, 174503 (2004).
- ⁵⁷P. Canfield, S. Bud'ko, and D. Finnemore, *Physica C* **385**, 1 (2003).
- ⁵⁸H. Yang, C. Ren, L. Shan, and H.-H. Wen, *Phys. Rev. B* **78**, 092504 (2008).